Large-Spacing Segmented Transmitter Track for Dynamic Wireless Power Transfer with Low Output Fluctuation

Hai Xu, *Member, IEEE*, Jingyu Wang, *Student Member, IEEE*, and Zhicong Huang, *Senior Member, IEEE*

***Abstract*—In segmented dynamic wireless power transfer (DWPT) systems, achieving a large spacing distance between adjacent transmitter pads while minimizing output power fluctuation often poses a significant challenge. This paper presents a novel large-spacing segmented transmitter (Tx) track, incorporating rectangular-double-solenoidal pads (RDSPs). The RDSPs are alternately positioned and orthogonally excited to produce a nearly constant magnetic field for the receiver pad over a wide range of dynamic displacement. Consequently, the proposed Tx track achieves both a large-spacing design and minimal output power fluctuation. Notably, the proposed design achieves a 107% spacing distance between adjacent Tx pads and maintains output power fluctuation below 4%, marking a substantial improvement compared to existing methods. This advancement significantly reduces the copper and ferrite requirements in DWPT systems. Furthermore, as the proposed approach operates without reliance on detection and control mechanisms, it theoretically imposes no limitation on the receiver pad's moving speed. A comprehensive optimal design methodology for the Tx track, accompanied by a detailed design flowchart, is provided. The effectiveness of the proposed design is validated through a 1 kW DWPT experimental prototype.**

***Index Terms*—Large-spacing, dynamic wireless power transfer, lower output power fluctuation, segmented transmitter track.**

I. Introduction

Dynamic wireless power transfer (DWPT) allows electric vehicles (EVs) to acquire power while in motion. Thus, it is a promising technology to overcome driving range anxiety or eliminate the necessity of configuring heavy batteries for EVs. The DWPT systems are expected to operate satisfactorily with stable output characteristics over a wide range of displacement.

To mitigate the fluctuations of output power and power efficiency during the DWPT process, consistent magnetic coupling irrespective of the dynamic displacement should be designed. According to the sizes of transmitter pad and receiver pad, the magnetic couplers in the DWPT systems can be classified into two categories. The first is long-track type [1]–[4], as shown in Fig. 1(a). In this design, the length of transmitter pad is significantly longer than that of the receiver pad [5], such as I-type [6], S-type [7], and N-type [8]. These long-track type designs can provide a continuous uniform magnetic field to achieve a constant coupling coefficient against the dynamic displacement, and thus simplify the circuit and control designs. However, a disadvantage of this long-track design is the comparatively low coupling coefficient, which significantly degrades the power efficiency to a noticeable extent and also gives rise to considerable electromagnetic exposure. To improve the coupling performance and suppress electromagnetic exposure, the second approach, termed as segmented design, is developed [9]–[12]. Compared with the long-track type, this approach includes multiple Tx pads that have nearly identical sizes to the Rx pad to optimize the coupling coefficient. Nevertheless, there still exist two challenges as follows.

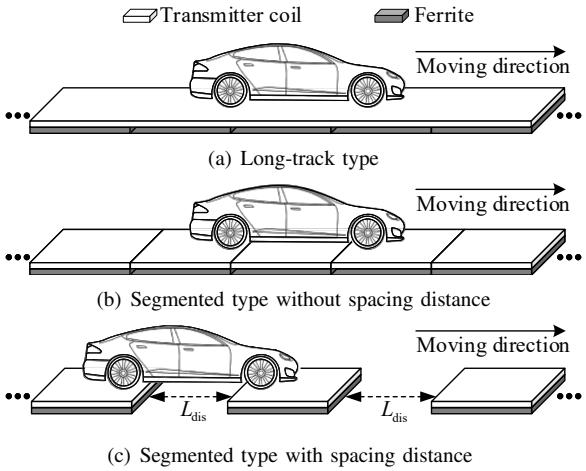

Fig. 1. Typical transmitter track types in DWPT systems.

1) Output power fluctuation due to the spacing zone between the adjacent Tx pads, and
2) Cross-coupling between the adjacent Tx pads.

To establish a uniform coupling magnetic field and achieve low power fluctuation against the wide-range displacement in segmented DWPT systems, continuous segmented Tx tracks without spacing distance have been widely studied, as illustrated by Fig. 1(b). In this way, the adjacent Tx pads of the segmented Tx track are designed without spacing. Ref. [13] uses rectangular coils wound overlap as the segmented Tx track. In Refs. [14], [15], array rectangular pads without spacing distance are constructed as a segmented track, while Ref. [16] allocates DD continuously as a segmented track. Moreover, an integrated design method based on the continuous elongated Tx rectangular pads is proposed [17]. Although these segmented tracks without spacing distance

Hai Xu, Jingyu Wang and Zhicong Huang are with the Shien-Ming Wu School of Intelligent Engineering, South China University of Technology, Guangzhou, 510006, China (e-mail: zhiconghuang@scut.edu.cn).

Digital Object Identifier TXXXxxxx.0000.0000.0000

can readily enhance the magnetic field between adjacent Tx pads and suppress the power fluctuation, the cross-coupling issue is severe. Such that, complex parameter designs for compensation networks [14], auxiliary decoupling coils [15], or additional mutual conductor designs [18] may be required to alleviate the cross-coupling issue. Moreover, it is noteworthy that continous placement of the Tx pads without spacing distance also indicates a heavy usage in magnetic core and wire.

It is straightforward to reduce the cross-coupling between adjacent Tx pads and achieve a cost-efficient design by configuring a segmented transmitter track with large-spacing between adjacent Tx pads, as shown in Fig. 1(c). However, such large-spacing designs have a common challenge, i.e., power fluctuation over the spacing region due to the decrease of magnetic coupling, which can be observed in recent research works [19]–[22]. For example, the power fluctuation reaches 50% when the distance between adjacent Tx pads is about 30% of the length of the Tx pad [22]. If the spacing distance is large to some extent, null-coupling phenomena may even be observed when the Rx pad is right above the spacing zone [20]. It is possible to modify the Rx pads to mitigate the power fluctuation by enlarging the Rx pad size or adopting a more complex strucutre [23]–[25]. For example, Ref. [25] wound solenoid coils around a long straight magnetic core plate to configure a bipolar-nonsalient pole Tx pad, while the Rx pad is designed with two much larger cross-tiled DD coils. However, this approach results in a more complex and cumbersome Rx side that demands much more installation space, which is usually not suitable for vehicle assembly in practice [26], [27].

Keeping simplifying the Rx pad in mind, our recent study has proposed an alternately-arranged arrangement segmented DWPT track, which allows a remarkable 50% spacing distance while achieving power fluctuation suppression [28]. However, due to inherent structural limitations, the magnetic field over the spacing zone of the adjacent Tx pads cannot be maintained constant and decreases rapidly if we continue to increase the spacing distance. Even though some efforts have been made to optimize the Tx pad parameters, the effect of improving the spacing distance is not significant. Therefore, stable output characteristics and large spacing distance between adjacent segmented Tx pads are still contradictory in segmented DWPT systems.

To this end, this paper is motivated to further investigate an improved Tx track design with larger spacing distance while maintaining low output power fluctuation. Subsequently, a rectangular-double-solenoidal pad (RDSP) structure is proposed to form a segmented Tx track, and 107% spacing distance between the adjacent Tx pads is achieved. In this way, the proposed segmented Tx track can further mitigate the cross-coupling issues and reduce copper usage and core consumption significantly due to the large-spacing configuration. Additionally, a comprehensive parameter analysis and optimal design methodology of the proposed Tx track, along with a detailed optimal design flowchart, is provided for further improving the array spacing and stability of the output characteristics.

TABLE I
PARAMETERS OF THE COUPLER

Symbols	Parameters	Value (mm)
l_{R}	Lenght of Rx rectangular coil	300
w_{R}	Width of Rx rectangular coil	300
l_{TS}	Lenght of double-solenoidal coil	306
l_{TR}	Lenght of Tx rectangular coil	300
w_{TR}	Width of Tx rectangular coil	300
l_{TF}, w_{TF}, d_{TF}	Ferrite dimensions of Tx pad	300, 300, 3
l_{RF}, w_{RF}, d_{RF}	Ferrite dimensions of Rx pad	300, 300, 3
d_{C}	Litz wire diameter of coils	3
h_{gap}	Power transfer gap distance	100
N_{TR}	Turn numbers of Tx rectangular coil	10
N_{R}	Turn numbers of Rx rectangular coil	10
P_{N}	Turn space of coils	0

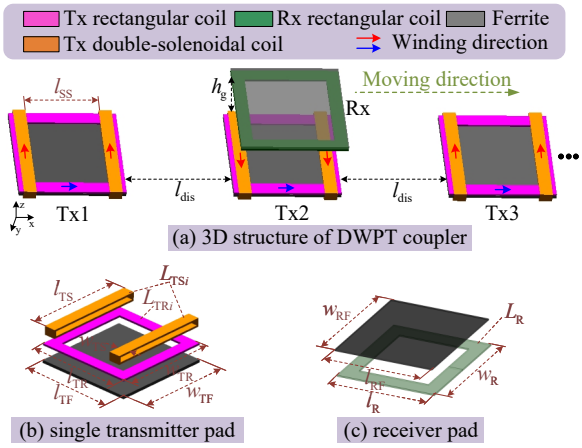

Fig. 2. 3D view of the proposed large-spacing DWPT Tx track based on RDSPs. Unless specified, subscripts TR, TSS, and R are used to indicate parameters of the Tx rectangular coil, Tx double-solenoidal coil, and Rx rectangular coil, while $i = 1, 2, 3$, etc. represents associated the Tx RDSP order.

The rest of this paper is organized as follows. Section II proposes and analyzes the working principle of a large-spacing segmented Tx track, then modelling the DWPT systems based on the proposed large-spacing segmented Tx track. Section III evaluates the key design parameter in the RDSP, then provides a comprehensive optimal design methodology of the proposed Tx track and a detailed design flowchart for further improving the array spacing and stability of the output characteristics. Section IV experimentally validates the proposed design and analysis and finally Section V concludes the paper.

II. Proposed Large-Spacing DWPT Segmented Track

A. Proposed Structural Design

Fig. 2 illustrated the configuration of the proposed large-spacing DWPT Tx track. The single pad on Tx side consists of a rectangular coil and a double-solenoidal coil, donated as rectangular-double-solenoidal pad (RDSP). As shown in Fig. 2(b), the double-solenoid coils are wound around the core in the symmetrical layout. Moreover, the double-solenoid coils are orthogonal layout with the rectangular coli, as a result, the coils on the Tx side are spatially integrated and magnetically decoupled. The proposed large-spacing DWPT

Tx track is based on segmented RDSPs with an alternate arrangement. As illustrated in Fig. 2(a), all the rectangular coils in the Tx RDSPs are wounded identically (marked with "→"), generating unified vertical magnetic flux right above the RDSPs. On the contrary, the double-solenoidal coils are wounded alternately. The odd double-solenoidal coils are wound in an anti-clockwise direction, while the even ones are wound clockwise (marked with "→"). Such that, the double-solenoidal coils generate alternating horizontal magnetic flux across the RDSPs. Thus, the magnetic generated from the rectangular coil and double-solenoidal coils are in complementary manner during the moving direction, which has been comprehensively demonstrated in our recently published work [28]. Only a single rectangular pad (RP) is designed on the Rx side, which can achieve minimization and lightweight, as shown in Fig. 2(c). Variable parameters of the proposed large-spacing DWPT coupler are summarized in Table I.

Since the double-solenoidal coil is woundentirely around the magnetic core, the relationship between the number of turns N_{TSS}, the design distance $l_{\mathrm{ss}}$of the double-solenoidal coil, and the length l_{TF} of the RDSP magnetic core should be satisfied as follow

$$2N_{\mathrm{TSS}}d_{\mathrm{C}} + l_{\mathrm{ss}} \leq l_{\mathrm{TF}}, \tag{1}$$

where d_{C} is the litz wire diameter of the coils.

With the abovementioned design of the Tx track, the Rx RP can capture vertical magnetic flux right over the RDSPs and also in the spacing zones, which are generated by the Tx rectangular coils and double-solenoidal coils respectively. The overall rectangular-to-rectangular mutual inductance is given by

$$M_{\mathrm{TR\text{-}R}} = M_{\mathrm{TR1\text{-}R}} + M_{\mathrm{TR2\text{-}R}} + \cdots + M_{\mathrm{TR}i\text{-}\mathrm{R}}. \tag{2}$$

Similarly, The overall double-solenoidal-to-rectangular inductance is given by

$$M_{\mathrm{TSS\text{-}R}} = M_{\mathrm{TSS1\text{-}R}} + M_{\mathrm{TSS2\text{-}R}} + \cdots + M_{\mathrm{TSS}i\text{-}\mathrm{R}}. \tag{3}$$

With the geometric specifications given in Table I, a finite element simulation is conducted in ANSYS Maxwell to simulate the proposed DWPT Tx track. As shown in Fig. 3, mutual coupling consistently exists as the Rx RP moves along the whole Tx track, but the situations are alternating in the spacing areas. In the odd spacing areas, $M_{\mathrm{TR\text{-}R}}$ and $M_{\mathrm{TSS\text{-}R}}$ are both positive and their slopes have a complementary tendency with the position change. However, in the even spacing areas, $M_{\mathrm{TR\text{-}R}}$ remains positive and axially symmetric to that in the adjacent spacing areas, but $M_{\mathrm{TSS\text{-}R}}$ is negative and centrally symmetric to that in the adjacent spacing areas. A straightforward way to tackle the abovementioned issue is by detecting the zero-crossing of $M_{\mathrm{TSS\text{-}R}}$ and using active control strategies. Such a scheme increases complexity and decreases robustness, making it less feasible in a practical DWPT system with many Tx RDSPs. In Section II-B, a purely passive way without complex detection and active control will be developed to achieve stable output.

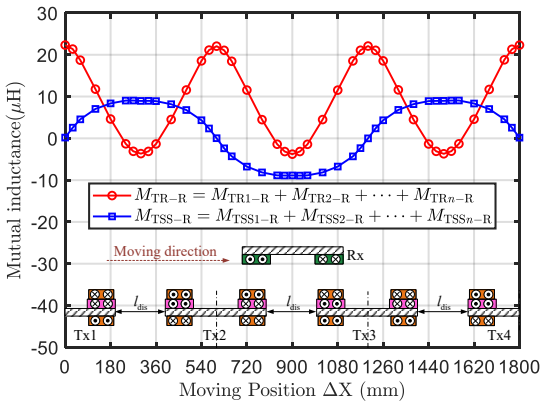

Fig. 3. Overall rectangular-to-rectangular and double-solenoidal-to-rectangular mutual inductances based on the proposed large-spacing segmented DWPT track.

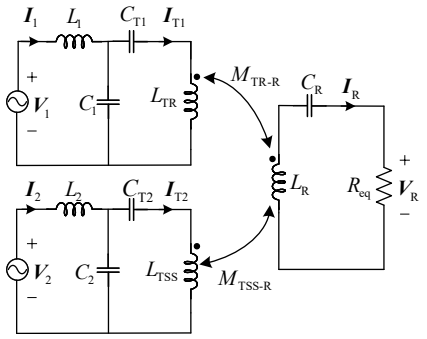

Fig. 4. Equivalent circuit of the proposed DWPT system based on large-spacing RDSP track.

B. Circuit Modeling

All Tx coils are compensated by LCC circuits, while the single Rx coil is series compensated. Thus, the weight and complexity of the Rx side can be reduced and simplified significantly. To catch the magnetic flux complementary feature of the proposed large-spacing DWPT coupler shown in Fig. 2 during the moving profile, the DWPT system should be designed to operate regardless of the mutual inductance $M_{\mathrm{TSS\text{-}R}}$ polarity without detections and control strategies. Such that, the Tx rectangular coils and the double-solenoidal coils are excited independently with an orthogonal excitation method. Taking this in mind and giving the neglect of the cross-coupling between the RDSPs, the equivalent schematics of the proposed DWPT system is shown in Fig. 4. The phase difference between AC voltage v_1 and v_2 is set to 90°. The fundamental harmonic approximation method has been utilized for analysis. The fundamental vector form relationship of $\boldsymbol{V}_1$ and $\boldsymbol{V}_2$ can be given as

$$\boldsymbol{V}_2 = \boldsymbol{V}_1 \angle 90^\circ = \frac{4}{\pi} V_{\mathrm{DC}} \angle 90^\circ. \tag{4}$$

Without loss of generality, $\boldsymbol{V}_1$, $\boldsymbol{V}_2$, $\boldsymbol{I}_1$, $\boldsymbol{I}_2$, $\boldsymbol{I}_{\mathrm{T1}}$, $\boldsymbol{I}_{\mathrm{T2}}$, and $\boldsymbol{I}_{\mathrm{R}}$ are corresponding fundamental vectors of v_1, v_2, i_1, i_2, i_{T1}, i_{T2}, and i_{R}, respectively. In addition, ω is the operating angle frequency. Parasitic resistances of the coils and the

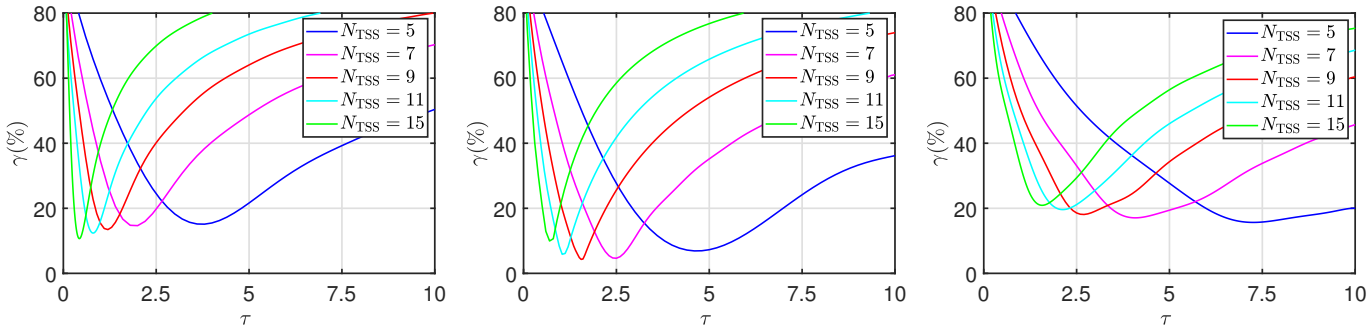

(a) N_{TSS} = 9, l_{ss} = 60 mm (b) N_{TSS} = 9, l_{ss} = 120 mm (c) N_{TSS} = 15, l_{ss} = 60 mm

Fig. 5. γ versus τ at different l_{ss} and N_{TSS} when the spacing $l_{\mathrm{dis}} = 240$ mm

compensation components are ignored to simplify the analysis. The circuit equations are given by

$$\begin{aligned} \boldsymbol{V}_1 &= X_1\boldsymbol{I}_1 - X_1'\boldsymbol{I}_{\mathrm{T1}} \\ 0 &= (X_{\mathrm{TR}} + X_1')\boldsymbol{I}_{\mathrm{T1}} - j\omega M_{\mathrm{TR\text{-}R}}\boldsymbol{I}_{\mathrm{R}} - X_1'\boldsymbol{I}_1 \\ \boldsymbol{V}_2 &= X_2\boldsymbol{I}_2 - X_2'\boldsymbol{I}_{\mathrm{T2}} \\ 0 &= (X_{\mathrm{TS}} + X_2')\boldsymbol{I}_{\mathrm{T2}} - j\omega M_{\mathrm{TSS\text{-}R}}\boldsymbol{I}_{\mathrm{R}} - X_2'\boldsymbol{I}_2 \\ 0 &= X_{\mathrm{R}}\boldsymbol{I}_{\mathrm{R}} - j\omega M_{\mathrm{TR\text{-}R}}\boldsymbol{I}_{\mathrm{T1}} - j\omega M_{\mathrm{TSS\text{-}R}}\boldsymbol{I}_{\mathrm{T2}} \end{aligned}, \quad (5)$$

where

$$\begin{aligned} X_1 &= j\omega L_1 + \frac{1}{j\omega C_1}, X_1' = \frac{1}{j\omega C_1} \\ X_{\mathrm{TR}} &= j\omega L_{\mathrm{TR}} + \frac{1}{j\omega C_{\mathrm{T1}}} \\ X_2 &= j\omega L_2 + \frac{1}{j\omega C_2}, X_2' = \frac{1}{j\omega C_2} \\ X_{\mathrm{TS}i} &= j\omega L_{\mathrm{TSS}} + \frac{1}{j\omega C_{\mathrm{T2}}} \\ X_{\mathrm{R}} &= j\omega L_{\mathrm{R}} + \frac{1}{j\omega C_{\mathrm{R}}} + R_{\mathrm{eq}} \\ R_{\mathrm{eq}} &= \frac{8}{\pi^2}R_{\mathrm{L}} \end{aligned}. \quad (6)$$

The compensation components L_1, C_1, L_2 and C_2 in the Tx RDSPs together with the series resonant circuit (L_{R}, C_{R}) on the Rx side are designed to be fully resonant, satisfying

$$\omega^2 = \frac{1}{L_1C_1} = \frac{1}{L_2C_2} = \frac{1}{L_{\mathrm{R}}C_{\mathrm{R}}}. \quad (7)$$

With (4), (5), and (7), the currents flow Tx rectangular coils, Tx double-solenoidal coils of the proposed DWPT system can be calculated as

$$\begin{aligned} \boldsymbol{I}_{\mathrm{T1}} &= -j\omega C_1\boldsymbol{V}_1 \\ \boldsymbol{I}_{\mathrm{T2}} &= -j\omega C_2\boldsymbol{V}_2 = -j\omega C_2\boldsymbol{V}_1\angle 90^{\mathrm{o}}. \end{aligned} \quad (8)$$

It can be observed that the DWPT system is equivalent to being driven by two current sources, and the DC output voltage $\boldsymbol{V}_{\mathrm{O}}$ of the proposed DWPT systems can be derived as

$$V_{\mathrm{O}} = \omega^2 V_{\mathrm{DC}} C_1 \sqrt{M_{\mathrm{TR-R}}^2 + \tau M_{\mathrm{TSS-R}}^2}, \quad (9)$$

where τ is the square of the ratio of compensation capacitors C_2 and C_1, given by

$$\tau = \frac{C_2^2}{C_1^2}. \quad (10)$$

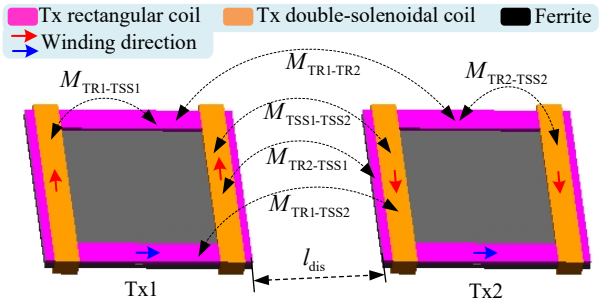

Fig. 6. Cross-coupling between the adjacent RDSPs.

With (10) and (9), the fluctuation of output voltage V_{O} is determined by M_{eq} given by

$$M_{\mathrm{eq}} = M_{\mathrm{TR\text{-}R}}^2 + \tau M_{\mathrm{TSS\text{-}R}}^2. \quad (11)$$

III. Analysis and Optimal Design of the RDSPs

A. Parameters Evaluation of RDSP for Power Fluctuation Suppression and Large-Spacing Design

As illustrated in Fig. 3, the mutual inductance $M_{\mathrm{TR\text{-}R}}$ and the $|M_{\mathrm{TSS\text{-}R}}|$ are in complementary manner. In the design process, the Tx and Rx rectangular coils are designed equally to maximize the coupling performance [29]. Moreover, the $M_{\mathrm{TSS\text{-}R}}$ is regarded as a mutual inductance to complement the $M_{\mathrm{TR\text{-}R}}$. Such that, we can optimal the double-solenoidal coil of the RDSP to achieve almost constant M_{eq} according to (11). One significant factor that affects the coupling effect of the WPT coupler is the number of turns and layout in the coil. Given that the coupler's structure and outer dimensions are fixed based on the design recommendations in SAE J2954 [30], the study of this part focuses on a design approach to improve the spacing between adjacent RDSPs and power fluctuation suppression for DWPT system via adjusting the double-solenoidal coil of the proposed RDSP DWPT coupler. In this design method, we concentrate on modifying the design distance (l_{ss}) and number of turns (N_{TSS}) in the double-solenoidal coil. The parameters of the rectangular coils are selected based on the design recommendations in SAE J2954 WPT1/Z1 [30], which are listed in Table I.

On the other hand, with (11), it is evident that there is a corresponding optimal threshold τ to minimize the fluctuation

TABLE II
THE OPTIMAL DESIGN POINTS WITH VARYING $l_{\rm ss}$ AND $N_{\rm TSS}$ UNDER DIFFERENT $l_{\rm dis}$.

$l_{\rm dis}$ = 240 mm					
$(\gamma\|_{\rm min},\tau)$ / $l_{\rm ss}$ \ $N_{\rm TSS}$	5	7	9	11	15
100 mm	(15.13%,3.8)	(14.67%,2.1)	(13.46%,1.3)	(12.32%,0.8)	(10.56%,0.5)
160 mm	(6.90%,4.6)	(4.29%,2.5)	(4.65%,1.6)	(5.86%,1.1)	(9.96%,0.7)
200 mm	(15.66%,7.3)	(17.11%,3.9)	(18.06%,2.7)	(19.61%,2.1)	(20.93%,1.6)
$l_{\rm dis}$ = 270 mm					
$(\gamma\|_{\rm min},\tau)$ / $l_{\rm ss}$ \ $N_{\rm TSS}$	5	7	9	11	15
100 mm	(26.16%,5.7)	(24.53%,2.9)	(23.18%,1.8)	(22.11%,1.2)	(18.94%,0.6)
160 mm	(5.39%,6.5)	(4.11%,3.5)	(3.01%,2.2)	(3.38%,1.6)	(4.53%,1.0)
200 mm	(8.09%,8.8)	(11.21%,3.2)	(12.16%,2.4)	(14.32%,1.8)	(21.88%,1.4)
$l_{\rm dis}$ = 300 mm					
$(\gamma\|_{\rm min},\tau)$ / $l_{\rm ss}$ \ $N_{\rm TSS}$	5	7	9	11	15
100 mm	(39.28%,6.5)	(37.54%,3.2)	(35.87%,1.8)	(34.58%,1.3)	(31.75%,0.8)
160 mm	(23.24%,7.6)	(21.27%,3.9)	(19.71%,2.5)	(18.06%,1.7)	(15.18%,1.0)
200 mm	(4.01%,11.6)	(3.03%,6.3)	(2.80%,4.1)	(3.90%,3.1)	(5.31%,2.3)
240 mm	(4.68%,14.8)	(5.93%,8.6)	(7.48%,6.0)	-	-

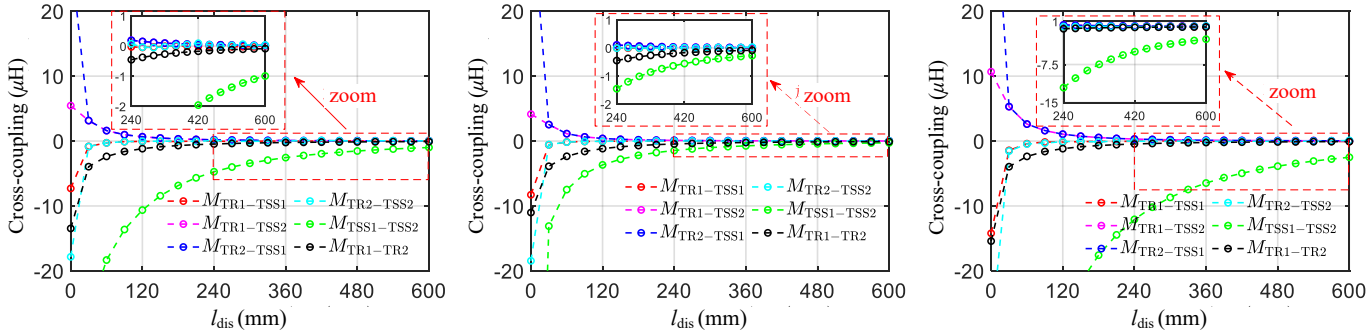

(a) $N_{\rm TSS}$ = 9, $l_{\rm ss}$ = 60 mm (b) $N_{\rm TSS}$ = 9, $l_{\rm ss}$ = 120 mm (c) $N_{\rm TSS}$ = 15, $l_{\rm ss}$ = 60 mm

Fig. 7. Cross-coupling between the adjacent Tx RDSPs versus $l_{\rm dis}$ at different $N_{\rm TSS}$ and $l_{\rm ss}$.

of $M_{\rm eq}$ after the mutual inductances $M_{\rm TR\text{-}R}$ and $M_{\rm TSS\text{-}R}$ designed. Subsequently, the fluctuation of the $M_{\rm eq}$ is defined as

$$\gamma = \frac{M_{\rm eq}|_{\rm Max} - M_{\rm eq}|_{\rm Min}}{M_{\rm eq}|_{\rm Max} + M_{\rm eq}|_{\rm Min}} \times 100\%. \tag{12}$$

Here $M_{\rm eq}|_{\rm Max}$ and $M_{\rm eq}|_{\rm Min}$ are the maximum and minimum values of $M_{\rm eq}$ versus the moving positions.

According to (12) and mutual inductance shown in Fig. 3, the fluctuation value γ with various τ under different $l_{\rm ss}$ and $N_{\rm TSS}$ are illustrated in Fig. 5. It can be advised that γ first decreases and then increases as a rise of τ. Thus, the minimum point represents the optimal design point with minimal fluctuations based on the given parameters in Table I, as shown in Fig. 5. The optimal design point with varying design distance ($l_{\rm ss}$) and number of turns ($N_{\rm TSS}$) in the double-solenoidal coil at different array spacing $l_{\rm dis}$ are listed in Table II.

As illustrated in Fig. 5 and Table II, it can be observed that the minimum fluctuation factor $\gamma|_{\rm Min}$ of the output voltage first decreases and then increases with an increase of $l_{\rm ss}$ when the $N_{\rm TSS}$ is designed. Thus there is an optimal design value of $l_{\rm ss}$ with the fixed $N_{\rm TSS}$, donated as $l_{\rm ss,opt}$. Additionally, when the $l_{\rm ss} < l_{\rm ss,opt}$, the $\gamma|_{\rm Min}$ decreases as the $N_{\rm TSS}$ increases. This

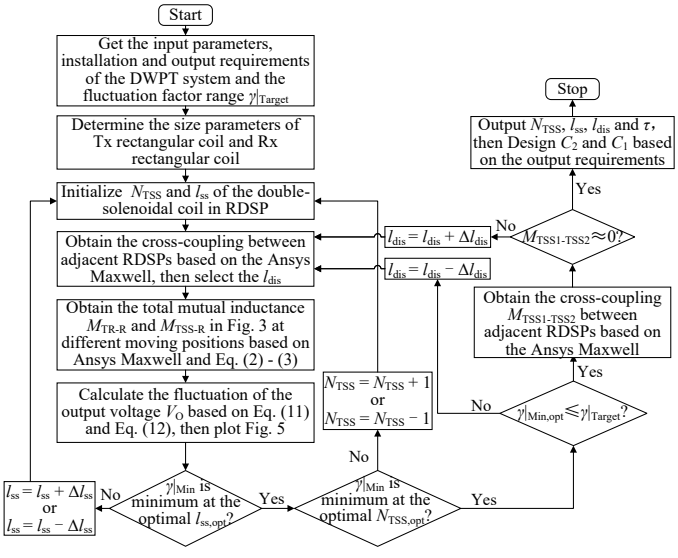

Fig. 8. Design flowchart for the proposed DWPT system.

indicates that we can improve the power fluctuation suppression of the proposed DWPT system by increasing the $N_{\rm TSS}$ if the $l_{\rm ss}$ is not enough. The $\gamma|_{\rm Min}$ raises as an increase of $N_{\rm TSS}$

when the $l_{\mathrm{ss}} > l_{\mathrm{ss,opt}}$, it demonstrates that increasing N_{TSS} will result in $M_{\mathrm{TSS\text{-}R}}$ in an overcompensation of $M_{\mathrm{TR\text{-}R}}$ if the l_{ss} has an enough design. At this time, the proposed RDSP is in the redundant design, i.e., excessive use of Litz wire and increased costs. However, when $l_{\mathrm{ss}} \approx l_{\mathrm{ss,opt}}$, the $\gamma|_{\mathrm{Min}}$ first decreases and then increases as a raise of N_{TSS}. Such that there is an optimal number of turns $N_{\mathrm{TSS,opt}}$ at the optimal design distance $l_{\mathrm{ss,opt}}$. Based on the aforementioned analysis, it can be concluded that the optimal design distance $l_{\mathrm{ss,opt}}$ should be obtained while keeping the number of turns N_{TSS} of the double-solenoidal coil unchanged in the optimal design process, and then redesigning the number of turns N_{TSS} under the condition of the optimal design distance $l_{\mathrm{ss,opt}}$.

B. Analysis of Cross-Coupling Issue

To mitigate circulating current, it is essential to minimize the cross-coupling between segmented Tx RDSPs. Although enlarging the spacing distance l_{dis} between Tx RDSPs can assist in reducing cross-coupling, it simultaneously intensifies power fluctuation. Therefore, a careful design is necessary. The major cross-coupling between the coils of the adjacent RDSPs is highlighted in Fig. 6. According to the FEA results, the cross-couplings between the neighboring Tx RDSPs versus l_{dis} at different N_{TSS} and l_{ss} are shown in Fig. 7. There is a significant initial decrease in the cross-couplings and the reduction becomes less pronounced as l_{dis} continues to increase until it reaches 240 mm, where most of the cross-couplings converge to zero. However, the cross-coupling between the adjacent double-solenoidal coils (e.g., $M_{\mathrm{TSS1\text{-}TSS2}}$ shown in Fig. 7) converges relatively slowly with the increase of the spacing l_{dis}. In addition, the $M_{\mathrm{TSS1\text{-}TSS2}}$ is sensitive to the number of turns N_{TSS} and the design distance l_{ss} of the double-solenoidal coil. Specifically, the increase of N_{TSS} or the decrease of l_{ss} will lead to the raise of $M_{\mathrm{TSS1\text{-}TSS2}}$, such that a larger spacing l_{dis} design is required to make it converge to zero.

Based on the aforementioned analysis, in order to eliminate or reduce the impact of cross-coupling on DWPT system, the number of turns N_{TSS} should be reduced as much as possible and the design distance l_{ss} should be increased during the design of the double-solenoidal coil while satisfying the power fluctuation suppression requirement. The cross-coupling of double-solenoidal coils in adjacent RDSPs (e.g., $M_{\mathrm{TSS1\text{-}TSS2}}$) is most pronounced with the same parameter design. Accordingly, to streamline the decoupled design process of the proposed segmented RDSPs transmitter and minimize time expenditure, the cross-coupling $M_{\mathrm{TSS}i\text{-}\mathrm{TSS}(i+1)}$ can be employed as a criterion. This entails that when the cross-coupling $M_{\mathrm{TSS}i\text{-}\mathrm{TSS}(i+1)}$ is approximately zero, it can be posited that the cross-coupling between adjacent RDSPs is essentially insignificant.

C. Optimal Design of the RDSPs

Given the aforementioned analysis, a design flowchart to detail the optimal design procedure and consideration for the proposed large-spacing DWPT segmented RDSP transmitter is shown in Fig. 8. Specifically, the design procedure of

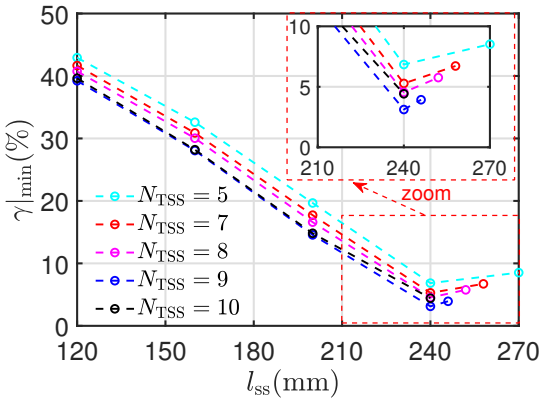

Fig. 9. Performance of $\gamma|_{\mathrm{Min}}$ at different l_{ss} and N_{TSS}.

TABLE III
PERFORMANCE OF $\gamma|_{\mathrm{Min}}$ AT $l_{\mathrm{ss,opt}}$ AND DIFFERENT N_{TSS}

Number of turns N_{TSS}	Optimal design point $(l_{\mathrm{ss,opt}}, \gamma|_{\mathrm{Min}})$
5	(240 mm, 6.84%)
7	(240 mm, 5.28%)
8	(240 mm, 4.54%)
9	(240 mm, 3.12%)
10	(240 mm, 4.42%)

the proposed large-spacing and power fluctuation suppression DWPT segmented RDSP transmitter can be summarized as follows.

1) Getting the input/output requirements (such as the input DC voltage, input power, operating frequency, the output voltage V_{O}, and output rated power, etc.) and setting the power fluctuation range $\gamma|_{\mathrm{Target}}$ of the DWPT system, Then, determining the parameters (i.e., the number of turns N_{TR}, N_{R}, and the Litz wire diameter d_{C}, etc.) of the Tx and Rx rectangular coils based on the input and output data. Initializing the number of turns N_{TSS} and the design distance l_{ss} of the double-solenoidal coil in the RDSP. Subsequently, analyzing the relationship between the cross-coupling in the adjacent RDSPs and their spacing l_{dis} via ANSYS Maxwell, as shown in Fig. 7. Selecting the preliminary spacing l_{dis} of the adjacent RDSPs under the cross-coupling variation characteristics in Fig. 7.
2) Obtaining the mutual inductances $M_{\mathrm{TR\text{-}R}}$ and $M_{\mathrm{TSS\text{-}R}}$ under different moving positions throughout the ANSYS Maxwell, as plotted in Fig. 3. Afterward, ultilizing the MATLAB to calculate the fluctuation factor γ versus the τ based on the Eq. (11) and Eq. (12), as well as the data of the $M_{\mathrm{TR\text{-}R}}$ and $M_{\mathrm{TSS\text{-}R}}$. Then plotting the Fig. 5. If the minimum fluctuation factor $\gamma|_{\mathrm{Min}}$ achieved under the optimal design distance $l_{\mathrm{ss,opt}}$, we can continue to obtain the optimal number of turns $N_{\mathrm{TSS,opt}}$ at the optimal design distance $l_{\mathrm{ss,opt}}$. Otherwise, the design distance l_{ss} is reinitialized, i.e., $l_{\mathrm{ss}} = l_{\mathrm{ss}} + \Delta l_{\mathrm{ss}}$ or $l_{\mathrm{ss}} = l_{\mathrm{ss}} - \Delta l_{\mathrm{ss}}$. Similarly, once the $\gamma|_{\mathrm{Min}}$ is identified as the value under the condition of the $l_{\mathrm{ss,opt}}$ and $N_{\mathrm{TSS,opt}}$, it can be recorded and donated as $\gamma|_{\mathrm{Min,opt}}$. Conversely, the number of turns N_{TSS} should be executed $N_{\mathrm{TSS}} = N_{\mathrm{TSS}} + 1$

or $N_{\mathrm{TSS}} = N_{\mathrm{TSS}} - 1$, and then redesigned.

3) When the fluctuation $\gamma|_{\mathrm{Min,opt}} > \gamma|_{\mathrm{Target}}$ achieves, reducing the spacing l_{dis} (i.e., $l_{\mathrm{dis}} = l_{\mathrm{dis}} - \Delta l_{\mathrm{dis}}$) of the adjacent Tx RDSPs and performing re-iterative design. However, if the fluctuation $\gamma|_{\mathrm{Min,opt}} \leq \gamma|_{\mathrm{Target}}$ satisfies, reconducting FEM analysis in ANSYS Maxwell to re-obtain the cross-coupling $M_{\mathrm{TSS}i\text{-}\mathrm{TSS}(i+1)}$ between the double-solenoidal coils in the adjacent Tx RDSPs. Once the cross-coupling $M_{\mathrm{TSS}i\text{-}\mathrm{TSS}(i+1)}$ is approximately equal to zero, output the optimal design value of l_{ss}, N_{TSS}, l_{dis}, and τ. Then designing the compensation capacitors C_2 and C_1 according to the output requirements. On the contrary, if the $M_{\mathrm{TSS}i\text{-}\mathrm{TSS}(i+1)} \neq 0$ and can not be ignored, the spacing l_{dis} should be increased (i.e., $l_{\mathrm{dis}} = l_{\mathrm{dis}} + \Delta l_{\mathrm{dis}}$) in accordance with Fig. 7 and redesigned.

Based on the above design flowchart, an optimal design example is provided in this section. The basic parameters as listed in Table I and the spacing $l_{\mathrm{dis}} = 320$ mm (about 107% of the proposed single RDSP length). The performance of the minimum fluctuation factor $\gamma|_{\mathrm{Min}}$ under different l_{ss} and N_{TSS} is shown in Fig. 9. It can be observed that the $\gamma|_{\mathrm{Min}}$ first decreases and then increases with the increase of design distance l_{ss} under different N_{TSS} conditions, moreover, the minimum point appears at the same design distance $l_{\mathrm{ss}} = 240$ mm. Therefore, the $l_{\mathrm{ss}} = 240$ mm is the optimal design distance $l_{\mathrm{ss,opt}}$. The corresponding minimum fluctuation factor $\gamma|_{\mathrm{Min}}$ under the optimal design distance $l_{\mathrm{ss,opt}}$ and different N_{TSS} is in detail in Table III. Obviously, the $\gamma|_{\mathrm{Min}}$ also possesses a minimum value point versus the N_{TSS} and achieves when the N_{TSS} is designed to be 9. Thus the value 240 mm and 9 is the corresponding optimal design distance $l_{\mathrm{ss,opt}}$ and number of turns $N_{\mathrm{TSS,opt}}$ respectively. With these optimal parameters, the fluctuation factor $\gamma|_{\mathrm{Min,opt}}$ is about 3.12% during the displacement of the DWPT system. Moreover, the maximum cross-coupling between the double-solenoidal coils in the adjacent RDSPs is 0.55 μH, which constitutes only a small percentage (2.3%) of that utilized for power transfer.

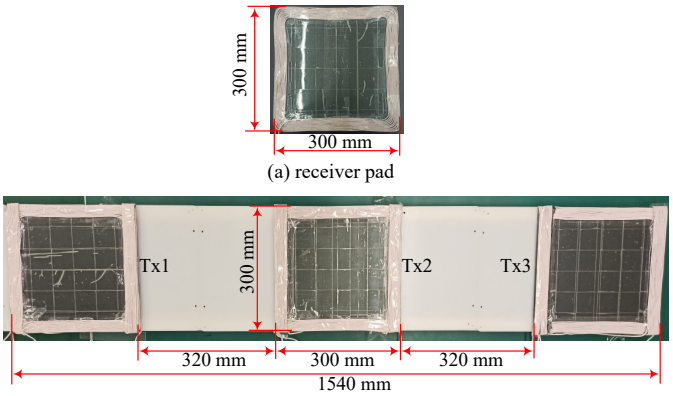

Fig. 10. Practical structure and dimension of proposed DWPT coupler.

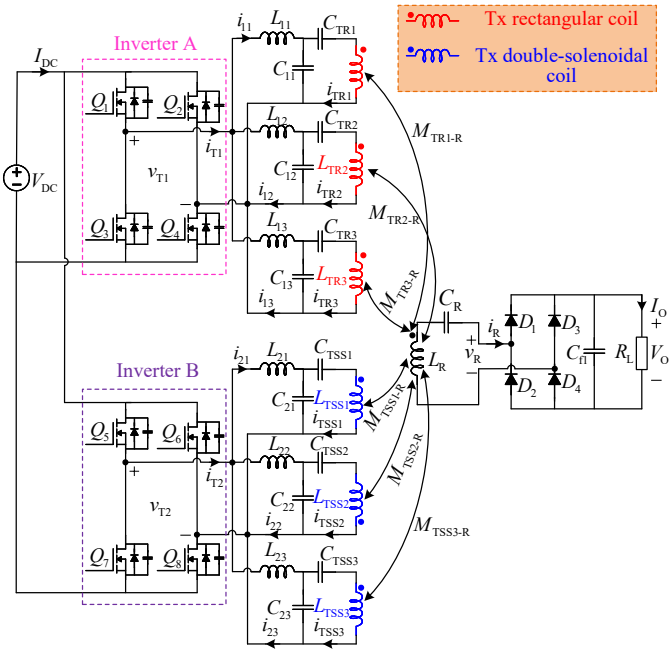

Fig. 11. Circuit configuration of proposed DWPT system.

IV. Experimental Verification

A. Experimental Setup

To verify the design and analysis of the proposed large-spacing RDSP coupler, a three-module scale-down 1 kW DWPT system laboratory prototype operating at 85 kHz switching frequency is built based on the schematic in Fig. 11, as depicted in Fig. 12. The proposed DWPT coupler, as shown in Fig. 10, is manufactured based on the configuration in Fig. 2 with the basic dimensions in Table I and optimal parameters provided in Section III-C. The material of the ferrite core is 3C95, which has permeability $\mu = 3000$ and is suitable for power transformers at frequencies up to 0.5 MHz. The geometry is plate type with size being $50 \times 50 \times 3$ mm^3. The magnetic core for the Tx and Rx pads consists of 6×6 pieces of ferrite cores and the overall size is $300 \times 300 \times 3$ mm^3. The Tx rectangular coils and the double-solenoidal coils are connected with LCC compensation network and orthogonal driven by independent inverters A and B respectively, as illustrated in Fig. 11. The two inverters share a digital controller (MCU Model: STM32F103). The controller generates two groups of PWM signals to drive the two independent inverters. The phase difference between these two group PWMs is set to be 90 degrees, such that it can achieve an orthogonal excitation between the two independent inverters. To simplify the design process, all the compensation conductors and corresponding capacitors of LCC networks for $L_{\mathrm{TR1}} - L_{\mathrm{TR3}}$ and $L_{\mathrm{TSS1}} - L_{\mathrm{TSS3}}$ are identically designed, i.e.,

$$\begin{aligned} L_1 = L_{11} = L_{12} = L_{13}, C_1 = C_{11} = C_{12} = C_{13} \\ L_2 = L_{21} = L_{22} = L_{23}, C_2 = C_{21} = C_{22} = C_{23} \end{aligned} \tag{13}$$

are satisfied.

The DC input voltage V_{DC} is fixed at 150 V, consequently, with the one-to-one voltage gain design, the required output voltage is also 150 V. A LCR meter (Model: HIOKI IM3536 is utilized to measure the mutual inductances ($M_{\mathrm{TR\text{-}R}}$,

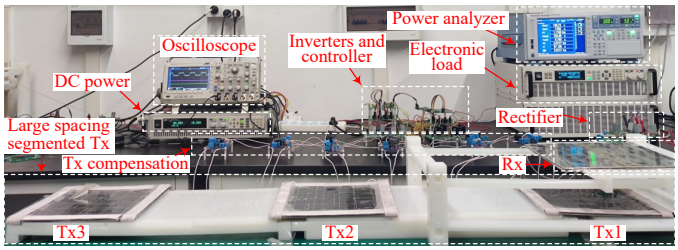

Fig. 12. Experimental prototype of 1 kW proposed DWPT system based on large-spacing segmented transmitter track.

TABLE IV
MEASURED PARAMETERS OF THE DWPT PROTOTYPE

Coupler parameters		Circuit parameters	
Symbols	Value	Symbols	Value
$L_{\mathrm{TR}i}$ (i=1,2,3)	95.61 μH, 96.14 μH, 95.58 μH	L_1, L_2	22.45 μH, 8.48 μH
$L_{\mathrm{TSS}i}$ (i=1,2,3)	97.06 μH, 96.86 μH, 98.65 μH	C_1, C_2	156.16 nF, 413.20 nF
L_{R}	96.32 μH	C_{R}	36.34 nF
h_{gap}	100 mm	$C_{\mathrm{TR}i}(i=1,2,3)$	44.43 nF, 44.13 nF, 44.30 nF
l_{dis}	320 mm (107%)	$C_{\mathrm{TSS}i}(i=1,2,3)$	39.22 nF, 39.31 nF, 38.53 nF
N_{TR}	10	V_{DC}	150 V
N_{TSS}	9	D_1 -D_4	MBR20200CTG
N_{R}	10	Q_1 -Q_8	STC 4050
l_{ss}	240 mm	f	85 kHz
d_{C}	3 mm	P_{O}	1 kW

$|M_{\mathrm{TSS\text{-}R}}|$, $M_{\mathrm{TSS1\text{-}TSS2}}$, $M_{\mathrm{TSS2\text{-}TSS3}}$) and self-inductances ($L_{\mathrm{TR}i}$, $L_{\mathrm{TSS}i}$, L_{R}). The measured total mutual inductances (i.e., $M_{\mathrm{TR\text{-}R}}$ and $|M_{\mathrm{TSS\text{-}R}}|$) and the cross-couplings (i.e., $M_{\mathrm{TSS1\text{-}TSS2}}$ and $M_{\mathrm{TSS2\text{-}TSS3}}$) of the practical coupler in Fig. 10 are illustrated in Fig. 13. It can be observed that the mutual inductance $M_{\mathrm{TR\text{-}R}}$ and $|M_{\mathrm{TSS\text{-}R}}|$ are in complementary manner during the displacement process, as shown in Fig. 13(a). The cross-coupling $M_{\mathrm{TSS1\text{-}TSS2}}$ and $M_{\mathrm{TSS2\text{-}TSS3}}$ of the double-solenoidal coils in the adjacent Tx1 – Tx3 RDSP is almost equal to zero, which can be ignored, as plotted in Fig. 13(b). Based on the data of measured mutual inductances in Fig. 13(a) and Eq. (11) - (12), the fluctuation γ versus τ is plotted in Fig. 14. The optimal design point can be achieved at τ = 7.0. Such that, with the input and output requirements mentioned above, the compensation parameters are designed and detailed in Table IV. The MOSFETs Q_1-Q_8 (Model: STC4050) are selected while the Rx rectifier (D_1-D_4) utilize diodes MBR20200CTG. A programmable DC electronic load (DH27605B) is employed to simulate a battery load, while the power analyzer YOKOGAWA WT1803E is used to measure the power distribution and the overall DC-DC efficiency of the proposed system.

B. Static Characteristics and Load-Independent Output Performance

Fig. 15(a) and (b) show experimental waveforms of modulated voltage v_{T1}, input current i_{T1}, modulated voltage v_{T2}, input current i_{T2}, induced voltage v_{R}, induced current i_{R}, output current V_{O}, and output voltage V_{O} at different moving

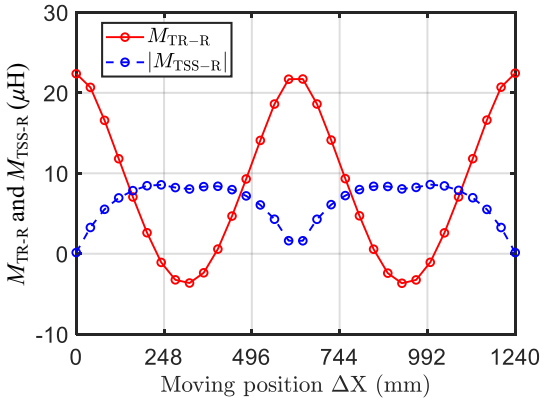

(a) ΔX= 0 mm

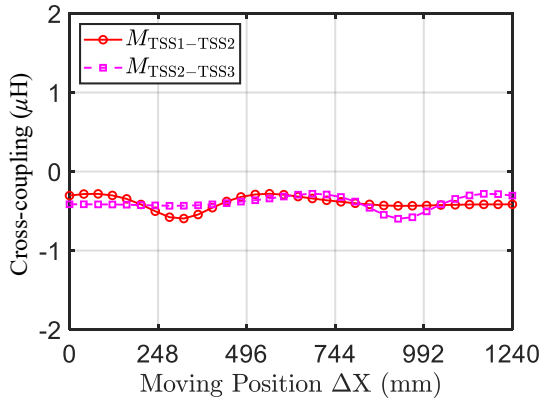

(b) ΔX= 0 mm

Fig. 13. Measured mutual inductance of the proposed large-spacing DWPT coupler under different displacement conditions during moving range ΔX $\in$ [0 mm 1240 mm]: (a) total mutual inductances $M_{\mathrm{TR\text{-}R}}$and $|M_{\mathrm{TSS\text{-}R}}|$, (b) cross-couplings $M_{\mathrm{TSS1\text{-}TSS2}}$and $M_{\mathrm{TSS2\text{-}TSS3}}$.

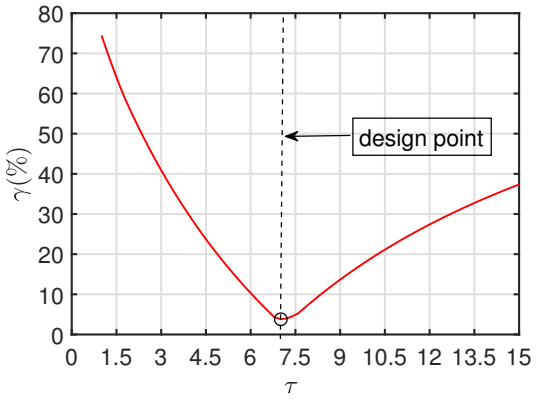

Fig. 14. The fluctuation value γ versus τ

positions ΔX= 0 mm and ΔX= 310 mm for full load with $R_{\mathrm{L}} = 22.5\ \Omega$. ΔX= 0 mm is the position that the receiver is fully aligned with the Tx1 while ΔX= 310 mm represents the position that the receiver arrives at the midpoint of the Tx1 and Tx2. It can be observed that the output voltage remains almost 150 V although the receiver moves to different positions. To evaluate the load-independent constant voltage (CV) output characteristic of the proposed DWPT system, a load variable

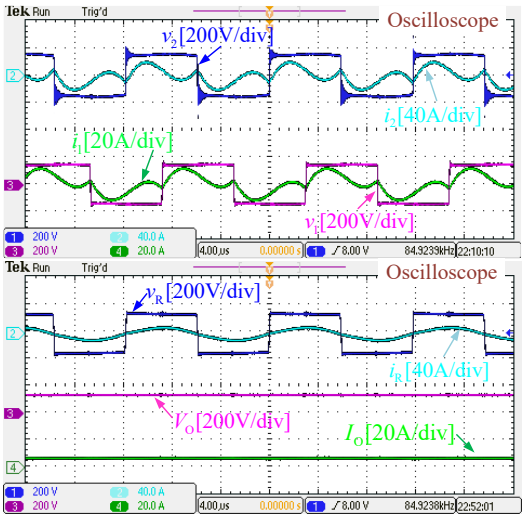

(a) ΔX= 0 mm

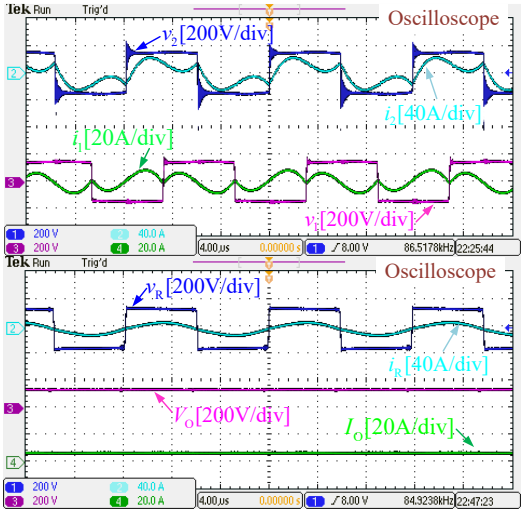

(b) ΔX= 310 mm

Fig. 15. Steady-state waveforms of the proposed DWPT system at different moving positions.

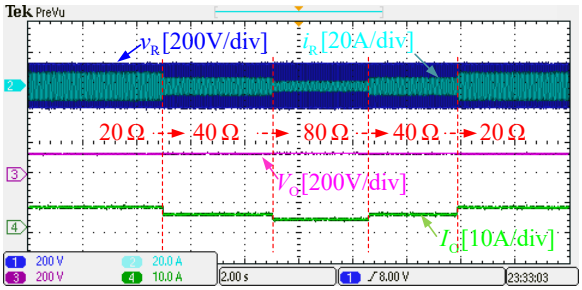

Fig. 16. Output voltages and currents under varying load conditions.

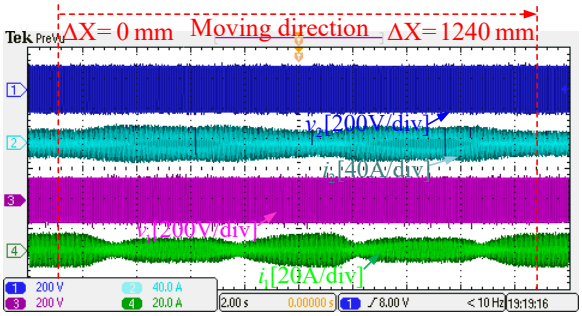

(a)

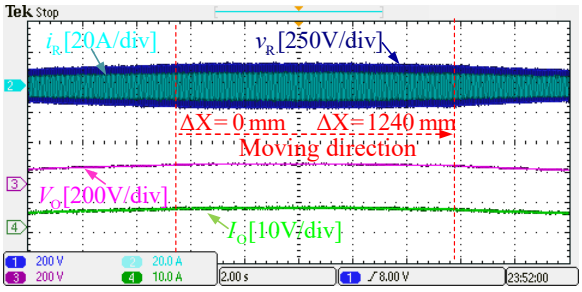

(b)

Fig. 17. Transient voltages and currents at full load: (a) transmitter side and (b) receiver side.

experiment is implemented at a position where the receiver pad arrives in the middle of Tx1 and Tx2 (i.e., ΔX= 310 mm), whereby the load is stepped from 20 Ω - 40 Ω - 80 Ω - 40 Ω - 20 Ω, as shown in Fig. 16. It can be observed that the output current I_O decreases as the load R_L increases, while the output voltage V_O remains almost constant. Therefore, the proposed DWPT system can achieve a good CV output feature.

C. Dynamic Performance

To evaluate the system's performance while the receiver pad moves across the entire section (i.e., moving position ΔX changes from 0 mm to 1240 mm), dynamic experiments are carried out for the full load $R_L = 22.5\ \Omega$, as shown in Fig. 17 (a) and (b) respectively. As illustrated in Fig. 17 (a), Channel 1 and 2 are the dynamic output voltage v_2 and output current i_2 waveform of the inverter B respectively, while the channel 3 and 4 are the dynamic output voltage v_1 and output current i_1 waveform of the inverter A respectively. It can be observed that the proposed DPWT system can operate in a smoothly complementary manner during the whole moving process to suppress the power fluctuation. From Fig. 17(b), it is obvious that the output voltage V_O at full load are consistent and almost constant during the moving profile. Fig. 18 provides the detailed V_O at full load for different moving positions along the moving direction. It should be noted that the fluctuation of the output voltage in the moving range ΔX ∈ [0 mm 1240 mm] is within 3.26%. Thus the proposed DWPT system possesses excellent power fluctuation suppression performance.

Fig. 19 illustrates the power efficiency measured by a power analyzer YOKOGAWA WT1803E at full load condition. It can be observed that the efficiency over the whole displacement range remains approximately stable at about 85%. Specifically, the minimum efficiency is 84.14% while the maximum one is 86.88%.

D. Comparison and Discussion

To further highlight the advantage, a detailed comparison of this work and the Ref. [28] is illustrated in Table V. It can

TABLE V
COMPARISONS WITH REF. [28]

Works	Tx & Rx Pad Structure	Tx & Rx Pad Size (cm)	Spacing Distance (cm)	Spacing Distance over Tx Pad Size	Cross-Coupling / Power Transfer Coupling	Output Fluctuation
[28]	RSP & RP	30×30 & 30×30	15	50%	8.2%	$\leq 5.42\%$
This work	RDSP & RP	30×30 & 30×30	32	107%	2.3%	$\leq 3.26\%$

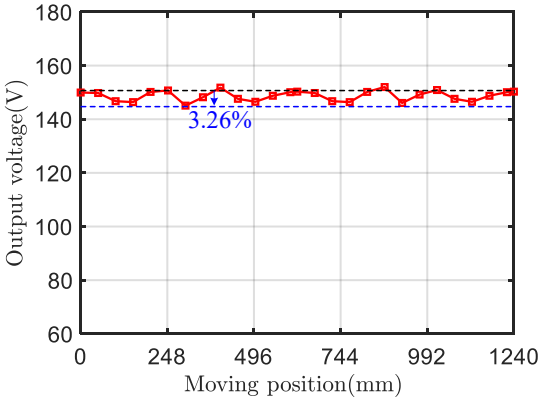

Fig. 18. Output voltage V_O at full load within moving range $\Delta X \in$ [0 mm 1240 mm].

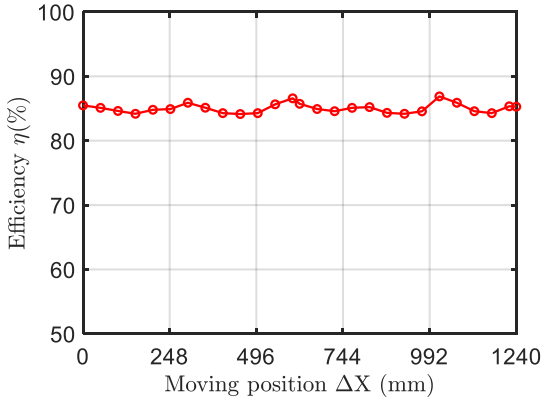

Fig. 19. Measured DC/DC efficiency of proposed DWPT system within moving range $\Delta X \in$ [0 mm 1240 mm] at full load.

be observed that both the design method in this paper and Ref. [28] can uniformize the size of Tx and Rx. However, the proposed design in this work achieves a large-spacing design with 320 mm (i.e. 107% of the individual Tx pad length) based on an optimal structure RDSP, while the spacing configuration in RSP segmented track in Ref. [28] is only 150 mm (i.e. 50% of the individual Tx pad length). Such that the proposed design further reduces approximately 37.3% in the utilization of copper and ferrite cores compared with the work in [28]. Due to the large spacing distance configuration between the adjacent Tx pads, it also further mitigates the cross-coupling issues. The maximum cross-coupling between the double-solenoidal coils in the adjacent RDSPs in this paper is only 0.55 μH, which constitutes only a small percentage (2.3%) of that utilized for power transfer. In addition, the output characteristic of the proposed large-spacing Tx segmented track possesses excellent stability. The output fluctuation is within 3.26% during the whole displacement process while the pulsation in [28] is 5.42%. Therefore, the stability of the proposed design in this paper is improved by 2.16%.

V. CONCLUSION

In this paper, a novel large-spacing transmitter (Tx) track is proposed, which consists of segmented rectangular-double-solenoidal pads (RDSPs). The proposed Tx track features a large-spacing design and excellent power fluctuation suppression performance during dynamic displacement simultaneously. The spacing between adjacent Tx RDSPs exceeds the single RDSP length, which achieves about 107% of the RDSP length. This significantly mitigates the cross-coupling issues and reduces the copper and ferrite requirements in DWPT systems. In addition, an optimal design methodology of the proposed Tx track, along with a detailed design flowchart, is introduced and analyzed comprehensively. A 1 kW DWPT experimental prototype using the proposed segmented Tx track and optimal design method is built to verify the analytical findings and design, and the experimental results demonstrate that the output voltage fluctuation is within 3.26% during displacement process while the spacing is 107% of RDSP length.

REFERENCES

[1] W. Zhang, S. C. Wong, C. K. Tse, and Q. Chen, "An optimized track length in roadway wireless power transfer systems," *IEEE J. Emerg. Sel. Topics Power Electron.*, vol. 2, no. 3, pp. 598–608, Sept. 2014.

[2] S. Song, Q. Zhang, Z. He, H. Li, and X. Zhang, "Uniform power dynamic wireless charging system with i-type power supply rail and dq-phase-receiver employing receiver-side control," *IEEE Trans. Power Electron.*, vol. 35, no. 10, pp. 11205–11212, Oct. 2020.

[3] V. B. Vu, M. Dahidah, V. Pickert, and V. T. Phan, "A high-power multiphase wireless dynamic charging system with low output power pulsation for electric vehicles," *IEEE J. Emerg. Sel. Topics Power Electron.*, vol. 8, no. 4, pp. 3592–3608, Dec. 2020.

[4] J. Wang, L. Wan, C. Cai, M. Xue, Y. Du, and J. Zhang, "A dual-side magnetic integration-based receiver detection method of long-track dwpt system," *IEEE Trans. Power Electron.*, vol. 39, no. 6, pp. 7752–7765, Jun. 2024.

[5] R. Tavakoli, E. M. Dede, C. Chou, and Z. Pantic, "Cost-efficiency optimization of ground assemblies for dynamic wireless charging of electric vehicles," *IEEE Trans. Transport. Electrific.*, vol. 8, no. 1, pp. 734–751, Mar. 2022.

[6] J. Huh, S. W. Lee, W. Y. Lee, G. H. Cho, and C. T. Rim, "Narrow-width wireless power transfer system for online electrical vehicles," *IEEE Trans. Power Electron.*, vol. 26, no. 12, pp. 3666–3679, Dec. 2011.

[7] S. Y. Choi, S. Y. Jeong, B. W. Gu, G. C. Lim, and C. T. Rim, "Ultraslim s-type power supply rails for roadway-powered electric vehicles," *IEEE Trans. Power Electron.*, vol. 30, no. 11, pp. 6456–6468, Nov. 2015.

[8] Z. Wang, S. Cui, S. Han, K. Song, C. Zhu, M. L. Matveevich, and O. S. Yurievich, "A novel magnetic coupling mechanism for dynamic wireless charging system for electric vehicles," *IEEE Trans. Veh. Technol.*, vol. 67, no. 1, pp. 124–133, Jan. 2018.

[9] J. P. K. Sampath, D. M. Vilathgamuwa, and A. Alphones, "Efficiency enhancement for dynamic wireless power transfer system with segmented transmitter array," *IEEE Trans. Transport. Electrific.*, vol. 2, no. 1, pp. 76–85, Mar. 2016.

[10] R. Tavakoli, T. Shabanian, E. M. Dede, C. Chou, and Z. Pantic, "Ev misalignment estimation in dwpt systems utilizing the roadside charging pads," *IEEE Trans. Transport. Electrific.*, vol. 8, no. 1, pp. 752-766, Mar. 2022.

[11] X. Gao, S. Dong, Y. Yin, Y. Zhang, and S. Cui, "An economical dwpt system with mutual compensation of segmented power supply rails based on lcl topology," *IEEE Trans. Transport. Electrific.*, vol. 9, no. 2, pp. 2865–2877, Jun. 2023

[12] S. Inoue, S. Kiguthi, J. Newman, T. Goodale, C. R. Teeneti, B. Hesterman, A. Kamineni, R. A. Zane, "50 kW reflexive tuning networks with low uncoupled transmitter currents for dynamic inductive power transfer systems," *IEEE Open J. Power Electron.*, vol. 5, pp. 436–451, 2024.

[13] C. Cai, M. Saeedifard, J. Wang, P. Zhang, J. Zhao, and Y. Hong, "A cost-effective segmented dynamic wireless charging system with stable efficiency and output power," *IEEE Trans. Ind. Electron.*, vol. 37, no. 7, pp. 8682–8700, Jul. 2022.

[14] F. Lu, H. Zhang, H. Hofmann, and C. Mi, "A dynamic charging system with reduced output power pulsation for electric vehicles," *IEEE Trans. Ind. Electron.*, vol. 63, no. 10, pp. 6580–6590, Oct. 2016.

[15] X. Li, J. Hu, H. Wang, X. Dai, and Y. Sun, "A new coupling structure and position detection method for segmented control dynamic wireless power transfer systems," *IEEE Trans. Power Electron.*, vol. 35, no. 7, pp. 6741–6745, Jul. 2020.

[16] W. Chen, F. Lin, G. A. Covic, and J. T. Boys, "Evaluation of a meandering track primary topology for ev roadway charging," *IEEE J. Emerg. Sel. Topics Ind. Electron.*, vol. 1, no. 1, pp. 26-35, Jul. 2020.

[17] K. Shi, C. Tang, H. Long, X. Lv, Z. Wang, and X. Li, "Power fluctuation suppression method for ev dynamic wireless charging system based on integrated magnetic coupler," *IEEE Trans. Power Electron.*, vol. 37, no. 1, pp. 1118–1131, Jan. 2022.

[18] S. A. Al Mahmud, I. Panhwar, and P. Jayathurathnage, "Large-area free-positioning wireless power transfer to movable receivers," *IEEE Trans. Ind. Electron.*, vol. 69, no. 12, pp. 12807–12816, Dec. 2022.

[19] H. Wang, U. Pratik, A. Jovicic, N. Hasan, and Z. Pantic, "Dynamic wireless charging of medium power and speed electric vehicles," *IEEE Trans. Veh. Technol.*, vol. 70, no. 12, pp. 12552–12566, Dec. 2021.

[20] K. Lee, Z. Pantic, and S. M. Lukic, "Reflexive field containment in dynamic wireless power transfer systems," *IEEE Trans. Power Electron.*, vol. 29, no. 9, pp. 4592–4602, Sept. 2014.

[21] S. Zhou and C. Chris Mi, "Multi-paralleled lcc reactive power compensation networks and their tuning method for electric vehicle dynamic wireless charging," *IEEE Trans. Ind. Electron.*, vol. 63, no. 10, pp. 6546–6556, Oct. 2016.

[22] J. M. Miller, P. T. Jones, J. Li, and O. C. Onar, "Ornl experience and challenges facing dynamic wireless power charging of ev's," *IEEE Circuits Syst. Mag.*, vol. 15, no. 2, pp. 40–53, May 2015.

[23] J. Liu, Z. Liu, W. Chen, X. Sun, and H. Su, "An optimized coil array and passivity-based control for receiving side multilevel connected dc-dc converter of dynamic wireless charging," *IEEE Trans. Veh. Technol.*, vol. 71, no. 4, pp. 3715–3726, Apr. 2022.

[24] C. Zhu, X. He, H. Yang, Y. Luo, B. Yang, J. Gao, R. Mai, and Z. He, "A magnetic field concentration enhanced i-shaped transmitter for dwpt system to achieve low power fluctuation," *IEEE Trans. Power Electron.*, vol. 39, no. 1, pp. 1690–1700, Jan. 2024.

[25] F. Zhao, S. Cui, C. C. Chan, and C. Zhu, "Modeling of high-efficiency non-salient pole transmitter in high-power dynamic wireless charging system for electric vehicles," *IEEE Trans. Power Electron.*, vol. 39, no. 7, pp. 8872–8882, Jul. 2024.

[26] N. P. C. Hanspeter Widmer and L. Sieber, "Wireless power antenna alignment adjustment system for vehicles," U.S. Patent US20110254503A1, 2011.

[27] W. Zhang, J. C. White, A. M. Abraham, and C. C. Mi, "Loosely coupled transformer structure and interoperability study for ev wireless charging systems," *IEEE Trans. Power Electron.*, vol. 30, no. 11, pp. 6356–6367, Nov. 2015.

[28] H. Xu and Z. Huang, "Alternately arranged segmented transmitter pads with magnetic field complementation for suppressing power fluctuation in dynamic wireless power transfer,"*IEEE Trans.Power Electron.*, vol. 39, no. 10, pp. 14091–14102, Oct. 2024.

[29] B. R. Long, J. M. Miller, A. Daga, P. C. Schrafel, and J. Wolgemuth, "Which way for wireless power: high q or high k?," in *Proc. IEEE PELS Workshop on Emerg. Technol.: Wireless Power Transfer (WoW)*, 2016, pp. 6–10.

[30] Hybrid - EV Committee, *Wireless power transfer for light-duty plug-in/electric vehicles and alignment methodology,* Warrendale, PA, USA: SAE Int., 2022.